

Structure and Unsteadiness of Swept-Ramp Shock Wave/Turbulent Boundary Layer Interactions



L. Vanstone and N. T. Clemens

Abstract In this study we investigate the flow structure and large-scale unsteadiness of a 3D shock wave/turbulent boundary layer interaction generated by a swept compression ramp in a Mach 2 flow. The unsteady dynamics of the flow are investigated using 50 kHz particle image velocimetry (PIV) in side-view and plan-view planes. The 50 kHz PIV velocity data are bandpass-filtered to investigate potential mechanisms that drive the large-scale unsteadiness. Our analysis shows that strong correlation exists between velocity fluctuations in the upstream boundary layer and motion of the separation-line surrogate for frequencies lower than 10 kHz ($0.25 U_\infty/\delta_{99}$). This frequency band correlates well with the characteristic frequency range of boundary layer superstructures. Separated flow motions in the high-frequency band (10–50 kHz) do not seem to be strongly correlated to the upstream flow, instead significant correlation is observed with structures within the separation region that move primarily in the cross-stream direction.

1 Introduction

Shock wave/boundary layer interactions (SWBLIs) are phenomena that are commonly experienced in high-speed flight and are associated with high-fluctuating pressure and heat loads [1, 2]. Of particular concern is the low-frequency unsteadiness, which is often associated with a number of very detrimental effects such as panel fatigue, inlet-isolator instability, buzz, and buffet. This unsteadiness has been widely reported in the literature to have timescales typically 10–100 times lower than the frequency (U_∞/δ_{99}) that characterizes the large-scale motions associated with the upstream boundary layer [3].

To date, the majority of research on large-scale unsteadiness has focused on 2D SWBLIs, such as those generated by unswept compression ramps and reflected

L. Vanstone · N. T. Clemens (✉)

Department of Aerospace Engineering and Engineering Mechanics, The University of Texas at Austin, Austin, TX, USA

e-mail: clemens@mail.utexas.edu

shocks, and much progress has been made toward understanding the causes of large-scale low-frequency unsteadiness [4–7]. A number of studies [6–10] find a relation between velocity fluctuations in the incoming boundary layer and the separated flow scale. Of particular relevance to this viewpoint are [8 and 9], which report that unsteadiness is linked to the presence of long ($30 \delta_{99}$) streamwise boundary layer superstructures located in the lower part of the upstream boundary layer. Furthermore, Poggie et al. [7] investigated SWBLI unsteadiness using flight data, wind-tunnel data, and numerical simulation data and found that the frequency spectra across all data sources collapse relatively well when appropriately normalized. They conclude that SWBLIs behave as a “selective amplifier of large-scale disturbances in the incoming flow”. They suggest that the type of unsteadiness they observe is consistent with a model recently put forward by Touber and Sandham [5].

However, other studies [4, 5, 11] have concluded that the dominant mechanism of unsteadiness of 2D interactions is intrinsic to the separated flow rather than arising from the upstream boundary layer. Some studies [4, 11] suggest that the separation bubble self-excites due to a mechanism associated with entrainment and recharge of the mass within the bubble. Very recently Priebe et al. [12] performed DMD analysis of a DNS of a SWBLI and showed that Görtler-like vortex structures that are generated within the interaction are linked to the low-frequency unsteadiness. Furthermore, Touber and Sandham [13] conducted an LES study of 2D interactions and showed that it is possible to observe large-scale SWBLI unsteadiness in the absence of boundary layer superstructures, which seems to indicate the dominance of a downstream mechanism.

The bulk of the above literature relates to unsteadiness in 2D interactions, but it is not known if the suggested mechanisms are relevant to 3D interactions, such as those generated by swept ramps and fins. A major difference between 2D and 3D interactions is that 2D interactions have a recirculating separation bubble and are thus termed “closed,” whereas swept interactions exhibit strong cross-flow that precludes recirculation and thus are termed “open” [14, 15]. Some models that have been proposed for large-scale unsteadiness seem to rely on the presence of a recirculating flow, and so such a mechanism may not be present in swept interactions. This study seeks to explore some of these issues and to add to our knowledge of the source of large-scale unsteadiness in swept SWBLIs.

2 Experimental Setup

2.1 Wind-Tunnel Facility

Experiments were conducted in the Mach 2 blowdown wind tunnel at The University of Texas at Austin. The test section was 0.152 m wide, 0.16 m tall, and 0.762 m long. Typical run times were 30 s with a stagnation pressure and temperature of 261 ± 7 kPa and 292 ± 5 K, respectively, and the freestream velocity was $U_\infty = 510$ m/s. In this study the coordinates x , y , and z refer to the streamwise, transverse, and cross-stream directions, respectively, as shown in Fig. 1. The

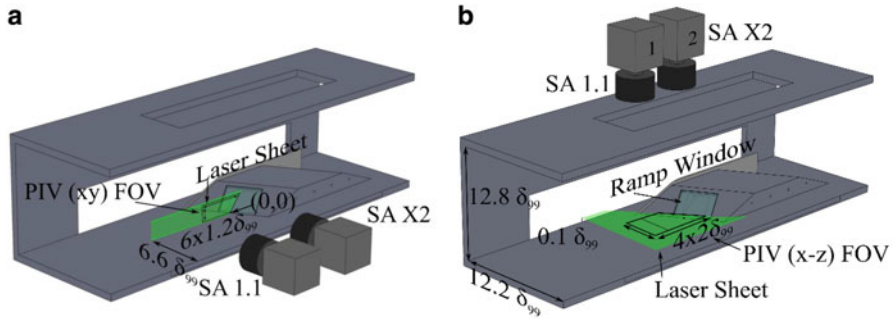


Fig. 1 Schematic diagrams of the swept ramp in the tunnel showing the experimental high-speed PIV configuration. (a) The x - y plane setup and (b) the x - z plane setup

respective velocity components are U , V , and W . The upstream boundary layer was turbulent with a velocity thickness (δ_{99}) of 12.5 mm for a boundary layer edge velocity of $0.99 U_\infty$. The compressible momentum (θ) and displacement (δ^*) thicknesses are 0.9 mm and 2.6 mm, respectively, the shape factor (H) is 2.89 and $Re_\theta = 34,200$ [19].

2.2 Windowed Swept Ramp

The test article used in this study was a swept compression ramp as shown in Fig. 1. The ramp was 101.6 mm wide, 25.4 mm high, and 280.0 mm long with a compression angle (α) of 22.5° and a sweep angle (ϕ) of 30° . The ramp was fitted with a single fence on the most upstream edge that extended 10 mm upstream and 3 mm in the y -direction to prevent interference from the tunnel corner flow. The center of the ramp was 82.5 mm ($6.6 \delta_{99}$) from the side of the tunnel closest to the downstream edge of the ramp. A window (25.4×25.4 mm) was fitted into the ramp face to enable passage of the laser sheet for side view (x - y) PIV. A side window enabled laser access for measurements in the x - z plane (Fig. 1b). For this experiment the origin (0,0) is considered to be on the midline of the ramp at the floor-ramp junction as shown in Fig. 1.

2.3 High-Speed Plan-View (x - z) Plane PIV

The high-speed (50 kHz) PIV system used a high-speed CMOS camera (FastCam SA 1.1) to view an upstream region of the incoming boundary layer and another (FastCam SA X2) to view the interaction region. Both cameras were operated at 100 kHz. The SA 1.1 was operated at a resolution of 384×128 px; the SA X2 was

operated at 384×264 px, and both were frame-straddled to match the pulse-doublet spacing. The laser source for the high-speed imaging was a frequency-doubled pulse-burst Nd:YAG laser (Spectral Energies QuasiModo). The laser produced 10 ms bursts of 500 evenly spaced pulse-doublets ($1.5 \mu\text{s}$ apart) at 50 kHz with a center wavelength of 532 nm. For plan-view PIV (x - z) (Fig. 1b) the same two cameras were used but viewed the flow through the top window. The laser sheet produced was approximately 0.5 mm thick and was positioned at $y = 0.075 \delta_{99}$. The PIV particles were titanium dioxide (TiO_2), which were seeded using a fluidized bed. LaVision DaVis v8 was used to process the PIV images. For PIV processing we used a multipass, adaptive interrogation scheme with an automatically adapting Gaussian weighted sub-pixel interpolation with a final window size of 32×32 px with an 87% overlap.

3 Results

3.1 Mean Structure of the Swept SWBLI

In previous work the mean structure of swept-ramp SWBLIs was investigated using surface flow visualization and low-speed PIV [16–18]. Sample surface flow visualization images are reproduced in Fig. 2. The images show a plan view (x - z) of the interaction, flow is left to right, and the ramp is on the right (the square structure is the ramp window). The flow visualization image shows the surface-streak lines in the upstream boundary layer, the upstream influence line, the separation line, separated flow streak lines, and the reattachment line. The swept nature of the interaction and the associated strong cross-flow component is evident. The dashed arrows in Fig. 2b show the surface streak lines inside the separation region.

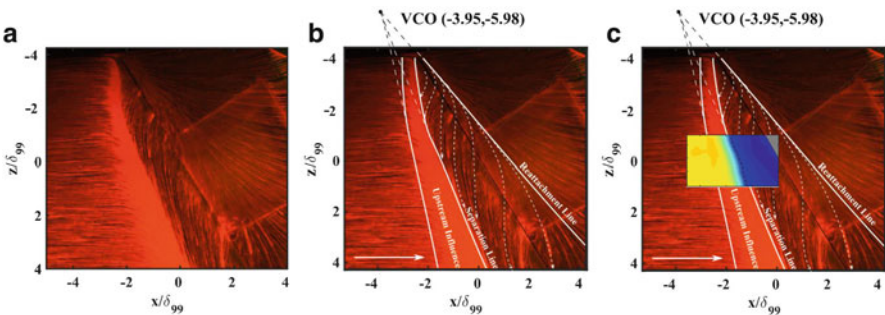


Fig. 2 Fluorescent surface flow visualization. (a) Sample image, (b) the same image with flow details annotated. Dashed arrows are surface streak lines, (c) the same image showing the plan-view PIV field of view. (From Ref. [16])

Swept SWBLIs are known to scale quasi-conically outside of the inception region, and Fig. 2 shows that this conical scaling is achieved once the separation and reattachment lines become straight. These lines can be traced to a single point, the virtual conical origin (VCO) [2, 20–23], as illustrated in Fig. 2b, c.

3.2 50 kHz Side-View PIV

Figure 3 shows a sequence of 50 kHz PIV images acquired in the x – y plane. The flow direction is left to right, and the images extend from just upstream of the line of upstream influence to just downstream of reattachment. The blue region designates low-velocity flow within the separated flow. A notable feature of the movies is that the separated flow is seen to undergo large-scale change from frame to frame – which implies that the frequency of large-scale separated flow unsteadiness is significantly higher than is typically attributed to 2D interactions [2]. This particular sequence was chosen as it demonstrates the “flapping” motion of the separation bubble. The flapping occurs by the growth of a structure in the shear layer, which leads to large vertical displacement of the shear layer and shedding of a large-structure near reattachment. This process is demonstrated several times in the

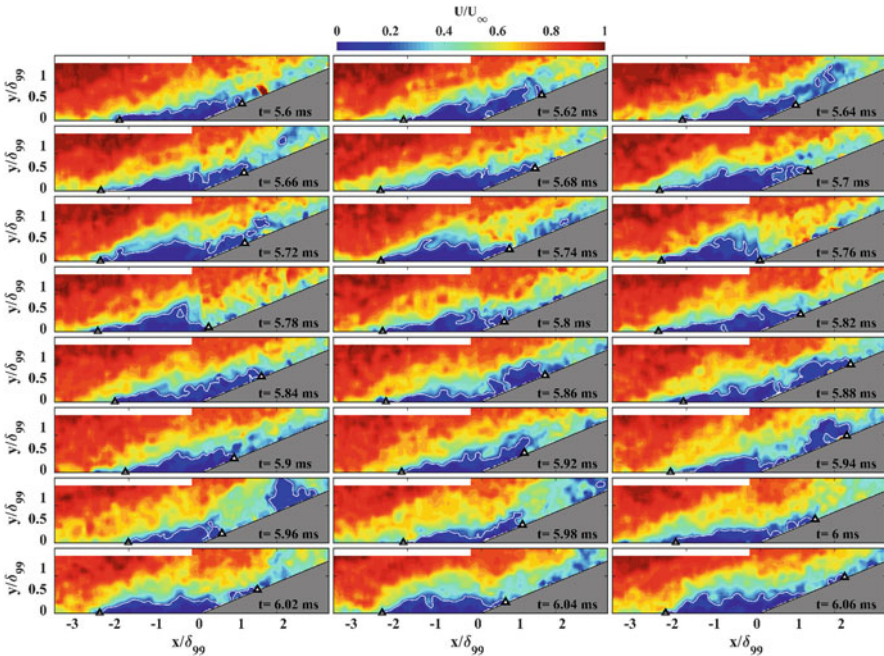


Fig. 3 A time-sequence extracted from the 50 kHz side-view PIV. The color map shows U -velocity contours. Flow is left to right

sequence. After shedding the structure, the reattachment location moves upstream rapidly, shrinking the separation region. This mechanism potentially accounts for some of the higher-frequency content in the separation region movement.

As in previous studies [16–18], we define a surrogate separation location because the PIV does not have adequate resolution to detect the true separation point, i.e., the point where the velocity gradient vanishes at the wall. We define the surrogate separation point as the farthest upstream location where the U-velocity drops below some threshold. We chose $0.2 U_\infty$ as this threshold to be consistent with previous studies. This location is shown by the upstream triangle near $y = 0$ in Fig. 3. A similar definition is used to define a surrogate reattachment point, i.e., the farthest downstream location where the velocity at the wall reaches a value of $0.2 U_\infty$. Note that the PIV cannot resolve these low velocities in the attached boundary layer. Inspection of the images shows that the surrogate separation point agrees well with the separation location that would be extracted “by eye.” The separation and reattachment points are indicated on each frame of the movie by triangle chevrons near the tunnel floor and ramp surface, respectively. Interestingly, the motion of the separation and reattachment points does not seem to be strongly correlated, which suggests that the separated flow does not “breathe” in a coherent fashion.

3.3 50 kHz Plan-View PIV

In the plan-view PIV (x - z plane), the laser sheet is located close to the wall ($0.075 \delta_{99}$) to enable better visualization of the separated flow region. The imaging field of view is shown in Fig. 2c. Figure 4 shows a time-sequence of U-velocity contours taken from the full dataset of 500 images acquired at 50 kHz. The field of view includes a section of undisturbed boundary layer and a cross section of the SWBLI, with the ramp face in the top right corner. The time between each frame is $20 \mu\text{s}$, during which the boundary layer convects approximately $0.5 \delta_{99}$. The incoming boundary layer is on the left, colored yellow-to-red in the color map. A small region ($x/\delta_{99} = -3.5$ to -2.5) of the incoming boundary layer is in the field of view. Broadly speaking the blue region shows a cross section of the separation region, and the turquoise region marks a cut through the shear layer. The surrogate separation line is marked on each plot as a solid black line. The time-average surrogate separation line is shown as a dashed line for reference.

The time-sequence in Fig. 4 begins ($t = 0$ ms) with a relatively upstream surrogate separation line near $z/\delta_{99} = 0.25$ and a relatively low-velocity inflowing boundary layer upstream of it. At $t = 0.08$ ms the beginning of a high-velocity superstructure [8, 9] is present at $z = 0.25 \delta_{99}$. Between $t = 0.08$ and 0.16 ms, this superstructure can be seen to impinge on the surrogate separation line, which seems to cause the separation line to recede downstream. At $t = 0.22$ ms a “blob” of

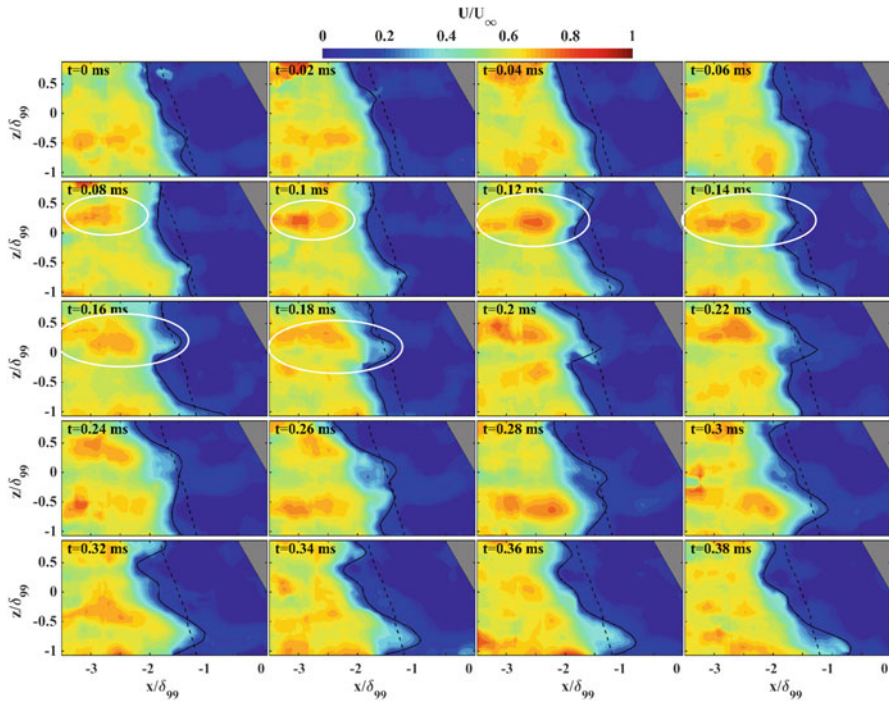


Fig. 4 A sequence extracted from the 50 kHz plan-view PIV. The contours show U-velocity contours. The instantaneous surrogate separation line is shown with a black line, average as a dotted line. Flow direction is left to right

higher speed (light blue) fluid can be seen in the separation region just downstream of the superstructure being examined (circled). Presumably it is a remnant of a superstructure that passed through the shear layer and was then entrained by the cross-flow. This blob of fluid can be seen to persist from approximately $t = 0.16$ ms to 0.30 ms. It is interesting to note that it remains relatively coherent for this duration. It is common to see these streamwise “bands” of high- and low velocity inside the separation region moving with the cross-flow through the separation region.

At approximately $t = 0.26$ ms, a second superstructure can be seen to come in at approximately $z = -0.5 \delta_{99}$. Much like the previously noted superstructure, once it enters the separated flow, it continues on a streamwise path for some time and can be seen to cause a significant local shrinking of the separation region, moving the surrogate separation downstream significantly.

4 Discussion

For the plan-view PIV, we now define the quantity L_{sep} , which for this study is taken as the distance from $x = 0$ to a point on the surrogate separation line. It should be noted that this is not the total separation length as the entire interaction is not visible. We also introduce the quantity U_{BL} as the average streamwise incoming velocity between $x = -3.5 \delta_{99}$ and $-2.8 \delta_{99}$. This quantity is averaged to help reduce the influence of high-frequency velocity fluctuations. This region is unaffected by the separated flow.

We now introduce two more quantities, δL_{sep} and δU_{BL} , which represent the relative changes in either quantity relative to the time-averaged quantities (which still vary with the span). Specifically, we make the following definition:

$$\delta L_{\text{sep}} = \frac{L_{\text{inst}} - L_{\text{avg}}}{\delta_{99}},$$

where L_{inst} is the instantaneous separation surrogate distance and L_{avg} is the time-average separation surrogate distance. The relation for δU_{BL} is defined as

$$\delta U_{\text{BL}} = \frac{U_{\text{BLinst}} - U_{\text{BLavg}}}{U_{\infty}},$$

where U_{BLavg} is the time-average of the line-averaged boundary layer velocity and U_{BLinst} is the instantaneous value of the line-averaged boundary layer velocity. These deviation quantities, δL_{sep} and δU_{BL} , can then be calculated for every point in the spanwise position of every frame for the entire dataset, giving approximately 30,000 data points. Analysis using these quantities can give an estimate of how the inflowing boundary layer momentum affects the separation location for the time-period examined. When both quantities are positive or both are negative, it would imply that the separation line is reacting to the incoming boundary layer velocity in line with the momentum argument made in Ref. [10].

4.1 Bandpass-Filtered Data

It has been shown here and previously [18] that the separated flow in this 3D SWBLI contains broadband frequency content. In order to further examine this content, the data are bandpass-filtered to extract the relative contributions of motions in three different frequency bands. The highest-frequency band (10–50 kHz) isolates unsteadiness mechanisms that are above the frequency of boundary layer superstructures. Boundary layer superstructures have been well-documented in our wind tunnel and have a length of approximately $10\text{--}30 \delta_{99}$ [17], which gives them a characteristic timescale of $0.25\text{--}0.75 \text{ ms}$ ($10\text{--}30 \delta_{99}/U_{\infty}$) and hence a frequency

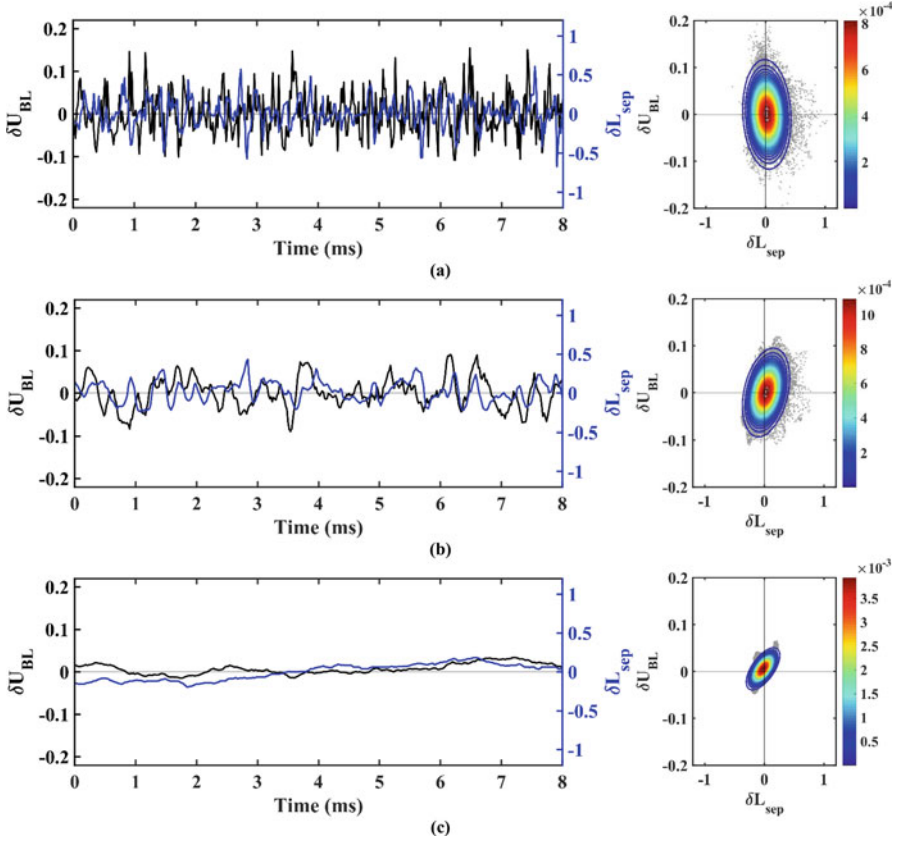


Fig. 5 Bandpass-filtered data. δL_{sep} and δU_{BL} time-history data at $z = 0$ (left) and a joint PDF of the entire data set (right) with all individual points overlaid (gray). (a) 10–50 kHz, (b) 1–10 kHz, and (c) 0–1 kHz. PDF contours represent percentage of dataset

range of approximately 1.3–4 kHz. Over the time range examined during a 10 ms, pulse burst about 10–30 superstructures might be expected to pass by a given x -location. Therefore, the mid-frequency band (1–10 kHz) highlights frequency content most likely to be associated with the boundary layer superstructures. The low-frequency band (0–1 kHz) highlights motions with frequencies below that of superstructures. These bandpass-filtered data are shown in Fig. 5: a time series of δL_{sep} and δU_{BL} at $z = 0$ is shown at left along with joint PDFs to examine the correlation among the two quantities shown at right. In the Fig. 5 time series, the black lines are $\delta U_{\text{BL}}(t)$, and the blue lines are $\delta L_{\text{sep}}(t)$. If the PDFs are tilted into the first and third quadrants, then this implies that positive upstream velocity fluctuations are correlated with downstream motion of the separation line. If the PDFs exhibit no tilt, then there is no correlation between the two quantities.

Figure 5a shows data for the highest-frequency band. The time history shows little correlation between δL_{sep} and δU_{BL} for a sustained period, and the joint PDF shows a slight negative tilt. The tilt is so small relative to the width of the PDF that we attribute no meaning to it and take this as evidence of virtually no correlation between the two variables. The amplitude of variation of δL_{sep} is large, which implies large-scale changes in the separated flow scale occurs for frequencies above 10 kHz. This observation was made qualitatively when considering Fig. 3 but is here made more definitive.

Figure 5b shows the contribution of the mid-frequency band, which is most likely associated with the boundary layer superstructures. The time histories at $z = 0$ show clear regions where δL_{sep} and δU_{BL} are correlated, a finding reflected in the tilt of the joint PDF. Further, the relative magnitude of changes in δL_{sep} is relatively large and comparable in size to the high-frequency content.

Figure 5c shows the result when the data have been low-pass filtered to 0–1 kHz, a frequency band that is below the characteristic frequency of the superstructures. This frequency band reveals the strongest correlation between δL_{sep} and δU_{BL} . In fact, the time series show that these quantities are approximately 180° out of phase. This observation is supported in the joint PDF in this subfigure, which displays the strongest tilt with the thinnest distribution but also a very low magnitude of variation of δL_{sep} . The low magnitude of δL_{sep} means that these lowest-frequency motions contribute the least to the large-scale changes in the separated flow.

4.2 High-Frequency Large-Scale Unsteadiness

As shown above, the high-frequency (10–50 kHz) content of the surrogate separation-line fluctuations (δL_{sep}) is weakly correlated with the inflowing boundary layer velocity fluctuations (δU_{BL}). In order to better understand the possible causes of this unsteadiness of the surrogate separation line, the high-frequency component of the PIV (10–50 kHz) is further investigated. In Fig. 4 a light-blue structure is highlighted by a white ellipse, and the structure is tracked from $t = 0.22$ ms until $t = 0.3$ ms. These types of structures are commonly seen to travel downward (in the crossflow direction) through the separation region.

Figure 6 shows x – t diagrams of δL_{sep} for a fixed z location. Figure 6a shows data that have been bandpass filtered to 10–50 kHz, and Fig. 6b shows data that have been bandpass-filtered to 1–10 kHz. Figure 6a shows the presence of quasiperiodic diagonal features, which persist for a fairly long time. Figure 6b shows these features are weaker in the 1–10 kHz band, and Fig. 6c shows they are completely absent from the 0–1 kHz band. The diagonal features imply that there are persistent high-frequency displacements (“ripples”) in the surrogate separation line that travel in the direction of the cross-flow. The velocity at which these ripples travel is about 82 m/s.

The surrogate separation-line ripples move with a velocity of about 82 m/s, which is less than the local fluid velocity of about 120 m/s. We further note that the

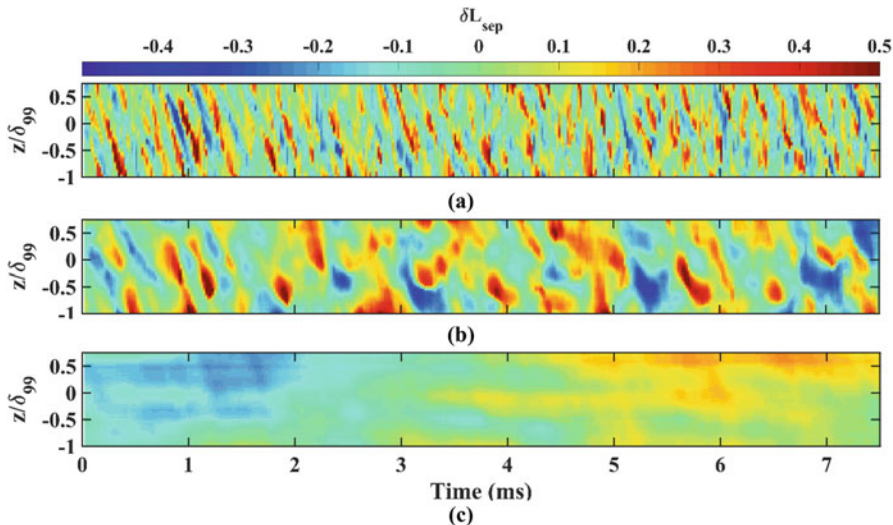


Fig. 6 $x-t$ diagrams of δL_{sep} for data that have been bandpass-filtered for the range: (a) 10–50 kHz, (b) 1–10 kHz, and (c) 0–1 kHz

propagation velocity of the ripples is nearly the same as the cross-flowing structures within the separated flow (such as those tracked in Fig. 4). Hence, we propose that the separated flow structures and surrogate separation-line ripples are likely the consequence of the same phenomenon. The fact that these structures travel with approximately 70–80% of the cross-flow velocity is reminiscent of rollers in a shear layer, which tend to move at the average of their two driving velocities. In this case the structures are rolling through the skewed shear layer that is created by the predominantly streamwise-directed flow above and the cross-stream-directed flow below. This is a new observation that suggests the presence of a high-frequency unsteadiness mechanism driven by the cross-flow shear. This observation seems to be consistent with the findings of Erengil and Dolling [24] that shock-foot unsteadiness shifts to higher frequencies as sweep (and hence cross-flow velocity) is increased.

5 Conclusion

This study forms part of an ongoing piece of work to explore unsteadiness mechanisms in a Mach 2 swept-ramp SWBLI. High-speed (50 kHz) PIV was used to acquire data in $x-y$ (streamwise-transverse) and $x-z$ (streamwise-spanwise) planes. The temporal resolution of the PIV is capable of resolving the large-scale motions of the flow.

The 50 kHz PIV movie sequences were bandpass-filtered into three frequency ranges: 0–1 kHz, 1–10 kHz, and 10–50 kHz. The midrange (1–10 kHz) overlaps the expected range of the upstream boundary layer superstructures. At the lowest-frequency band, the separated flow motion is highly correlated with velocity fluctuations in the upstream boundary layer, but its contribution to the magnitude of oscillation is smaller than for the higher-frequency bands. The mid-frequency band also shows a strong correlation with the upstream boundary layer, and the magnitude of the separation-line motion is large, which suggests that the superstructures play an important role in driving the large-scale unsteadiness. However, in the highest-frequency band (10–50 kHz), there is virtually no correlation between the upstream boundary layer fluctuations and large-scale separation-surrogate unsteadiness. Instead, unsteadiness in this frequency band was shown to be associated with propagating banded structures within the separation bubble that appear to be driven by the shear formed by the separated shear layer from above and the cross-flow from below.

Acknowledgments This work is sponsored by the US AFOSR under grant FA9550-14-1-0167 with Dr. Ivett Leyva as the program manager.

References

1. A.J. Smits, J.P. Dussauge, *Turbulent Shear Layers in Supersonic Flow* (AIP, Woodbury, 1996)
2. D.S. Dolling, *AIAA J.* **39**, 1517–1531 (2001)
3. M.E. Erengil, D.S. Dolling, *AIAA J.* **29**, 728–735 (1991)
4. S. Piponniau, J.P. Dussauge, J.F. Debiève, P. Dupont, *J. Fluid Mech.* **629**, 87 (2009)
5. E. Touber, N.D. Sandham, *J. Fluid Mech.* **671**, 417–465 (2011)
6. N.T. Clemens, V. Narayanaswamy, *Ann. Rev. Fluid Mech.* **46**, 469–492 (2014)
7. J. Poggie, N.J. Bisek, R.L. Kimmel, S. Stanfield, *AIAA J.* **53**, 1–15 (2015)
8. B. Ganapathisubramani, N.T. Clemens, D.S. Dolling, *J. Fluid Mech.* **585**, 369 (2007)
9. B. Ganapathisubramani, N.T. Clemens, D.S. Dolling, *J. Fluid Mech.* **636** (2009)
10. S.J. Beresh, N.T. Clemens, D.S. Dolling, *AIAA J.* **40**, 2412–2422 (2002)
11. S. Priebe, M.P. Martín, *J. Fluid Mech.* **699** (2012)
12. S. Priebe, J.H. Tu, C.W. Rowley, M.P. Martín, *J. Fluid Mech.* **807**, 441–477 (2016)
13. E. Touber, N.D. Sandham, *Theor. Comp. Fluid Dyn.* **23**, 79 (2009)
14. D. Knight, C. Horstman, S. Bogdonoff, B. Shapey, *AIAA J.* **25**, 1331–1337 (1987)
15. D. Knight, G. Degrez, Shock wave boundary layer interactions in high Mach number flows a critical survey of current numerical prediction capabilities. *Advis. Rep. 319*, AGARD, Neuilly sur Seine, vol. 2 (1998)
16. L. Vanstone, M. Saleem, S. Seckin, N.T. Clemens, *AIAA Paper 15–0622*, 45th AIAA Fluid Dynamics Conference, June (2015)
17. L. Vanstone, M. Saleem, S. Seckin, N.T. Clemens, *AIAA paper 2016–0104*, 54th AIAA Aerospace Sciences Meeting, January (2016)
18. L. Vanstone, M. Saleem, S. Seckin, N.T. Clemens, *AIAA Paper 2017–0757*, 55th AIAA Aerospace Sciences Meeting, January (2016)
19. Y. Hou, Particle Image Velocimetry Study of Shock Induced Turbulent Boundary Layer Separation, PhD Thesis. The University of Texas at Austin (2003)

20. G.S. Settles, D.S. Dolling, Paper AIAA 1990-375, AIAA 28th Aerospace Sciences Meeting (1990)
21. J.D. Schmisser, D.S. Dolling, AIAA J. **32**, 1151-1157 (1994)
22. F.S. Alvi, G.S. Settles, AIAA J. **30**, 2252-2258 (1992)
23. N. Arora, M.Y. Ali, Y. Zhang, F.S. Alvi, AIAA SciTech. (2015)
24. M.E. Erenkil, D.S. Dolling, AIAA J. **31**, 302-311 (1993)